
Article:
Lord, C.E. orcid.org/0000-0002-2470-098X and Rongong, J.A. orcid.org/0000-0002-6252-6230 (2016) A Tangential Microslip Model for Circularly and Elliptically Loaded Structures. Proceedings of the Institution of Mechanical Engineers, Part C: Journal of Mechanical Engineering Science , 230 (6). pp. 900-909. ISSN 0954-4062

https://doi.org/10.1177/0954406215608409

A tangential microslip model for circularly and elliptically loaded structures

Charles E Lord and Jem A Rongong

Department of Mechanical Engineering, Dynamics Research Group,
University of Sheffield, Sheffield, S1 3JD, United Kingdom
Email: c.lord@sheffield.ac.uk

Abstract

It is well known that the noise and vibration control of structures is a continuing challenge. With many structures this is commonly achieved through passive vibration damping; often using viscoelastic materials. It is sometimes however that the use of such materials is not permitted as their properties change over time, or when they are subjected to low and high temperature environments. For these structures and structural elements, it is often that clamping or applied boundary conditions are critical for providing the energy dissipation through microslip. This makes it necessary to understand the level of damping that arises from the clamping zones. In general, the estimation of damping is complicated in that most structures are not uni-directionally loaded and can have a planar path of motion (e.g. gas turbine blades, circular motion valves). Although it is typical during experiments and simulations to reduce a structure into a single axis of excitation, this can often be an over simplification which does not describe the dynamics of the system; but should be included. This paper presents a biaxial planar motion tangential microslip model that accounts for the vibratory loads arising from circular and elliptical motion. This model vectorially decouples and reduces the planar vibratory circular and elliptical motion into two separate independent tangential microslip models. The models account for tip loading and for centroid loading within the microslip region of the clamping zone. Each analytical microslip model is presented and is compared to numerical simulations using finite elements. The analytical models are then coupled to demonstrate the net effect that various eccentricities have on the overall energy dissipation

within the structure. The coupled models are then compared to numerical simulations using finite elements through ANSYS.

Keywords

Friction model, microslip, damping, hysteresis

1 Introduction

Typically, clamped joints express two different types of motion during vibrations: microslip and macroslip. When a tangential force is applied to a clamped joint small zones at the clamp initially break free and allow slipping to occur in localised areas; this is referred to as microslip. If the force is large enough, the microslip will propagate throughout the entire clamped joint and will result in gross slip; this is known as macroslip. In this paper, macroslip is not considered but rather focus is confined to purely microslip and therefore various friction models and stick-slip behaviour are not discussed.

Vibrational damping in most structures, without purpose-driven damping elements, is relatively small. This is especially true with metallic structures. The joints within these structures serve as a method that can be instigated for increasing the level of damping. For example, work done by Hartwigsen et al [1] has demonstrated experimentally the nonlinear effects from a beam with a shear lap joint. They showed that damping ratios could be greater than 0.03 depending on the exciting amplitude.

Although the use of joints as a method of promoting damping is not a new approach, there is still inadequate knowledge of how to model the behaviour of these structures accurately and, all importantly, how to design efficient structures utilising them. It is however well-recognised that the dynamic response of clamped joints is strongly affected by microslip. For these reasons further understanding is a necessity.

Previously, Menq et al [2,3] developed a one-dimensional microslip model with a bar and a platform where the friction layer was represented as an elastoplastic shear layer consisting of a series-

parallel-series model. They showed that with the correctly chosen parameters, their model predicted energy dissipation and matched experimentally obtained responses for a range of excitation frequencies and amplitudes. Following this work, Cigeroglu et al [4] proposed a similar model, differences being that this model included the inertia from the bar and that the normal force was non-uniform. They demonstrated that as the excitation frequency approached the natural frequency that the system began to soften. Using the Fourier coefficients, they then developed a point friction model. Xiao et al [5] studied the energy dissipation of a mechanical lap joint using the one-dimensional friction model developed by Menq et al [2]. They were interested in the contact interface tangential stiffness and pressure distribution laws on the energy dissipation at bolted joints. They demonstrated that as the pressure law coefficient increased, the stiffness decreased and as the elastic stiffness of the shear layer decreased that the hysteresis loops began to resemble a viscoelastic response. Sanliturk and Ewins [6] modelled the two-dimensional behaviour of a point friction contact using the harmonic balance method. Their proposed efforts were an extension of work from Menq et al [7]. One of the main differences from others is that in their model they were not limited to Coulomb friction while the friction force at the joint was accommodating to either experimental or theoretical data.

In this paper a two-dimensional clamped joint is considered that is exposed to circular and elliptical loading. Clamping with preload is applied on three sides around the perimeter of the clamp (detailed in Figure 2). A sinusoidal forcing function is applied for each direction (orthogonal) at the same frequency with a zero phase shift. This forcing function originates from the portion of the cantilever structure that extends beyond the clamped zone creating the tangential loading. The harmonic loading is considered to be small compared to the clamping preload force and therefore the coupling of the harmonic loading with the preload is ignored.

2 Mathematical model

The planar tangential model presented in this paper is coupled by two different and distinctive one-dimensional tangential models: tip loading and centre loading. The tip and centre loading are defined as axial loadings applied to the biased extreme boundary and applied to the centroid of a 2-D bar, respectively. Each of the tip loaded and centre loaded models are based on a backward finite difference approach to find the force-displacement response. The loads at the clamping zone originate from the inertial loads external to the clamping zone. The circular and elliptical motion is created depending on

$$R = \frac{F_{T(tip)}}{F_{T(centre)}}, \tag{1}$$

where F_T is the force being applied to the contact zone. The two-dimensional trajectories being considered are listed in Figure 1.

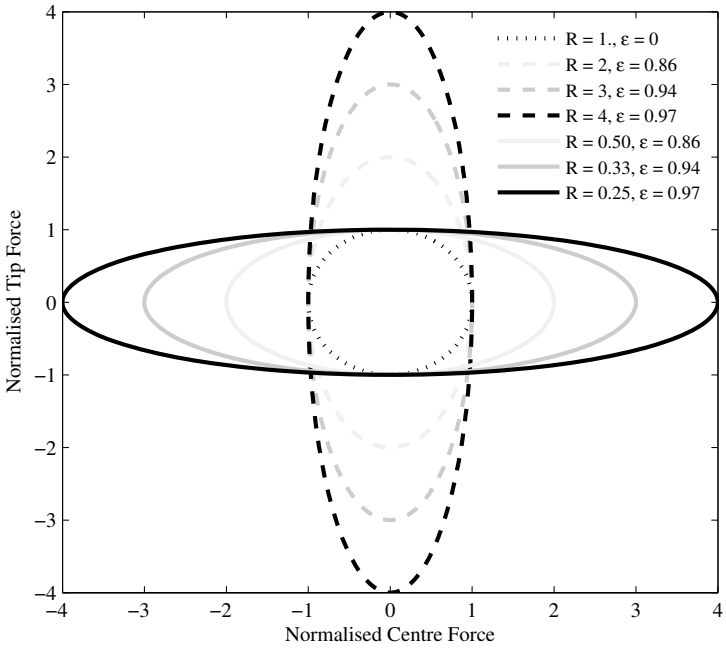

Figure 1: Normalised tip force to normalised centre force ratios, R, and eccentricities, ε, for various elliptical loading

Both the tip and centre loaded models ignore the clamped zone mass making the assumption that the external mass (or equivalent mass) is significantly larger. An example of this type of loading is shown in Figure 2.

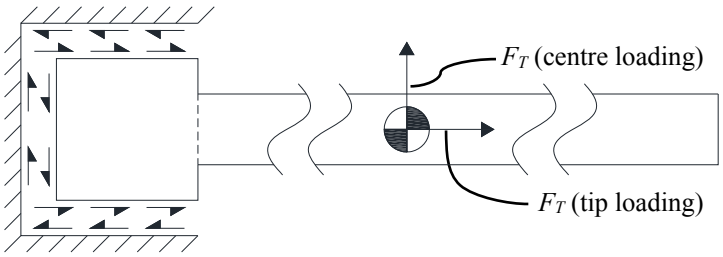

Figure 2: Two-dimensional tip and centre loading on clamping zone

The mass external to the clamped zone is assumed to act as a translational moving rigid body in both the tip and centre loading directions ignoring any bending. Shear deformations for the mass inside the clamped zone are ignored as they are relatively minute in amplitude.

For each simulation the preload (normal force) and coefficient of friction are considered to be constant. Furthermore, the static and dynamic friction coefficients are equal and any transition is neglected.

Since the loading for each of the models is perpendicular to the other, the notation of the geometric variables for the length, L, and thickness, t, requires a slight alteration. This is depicted in Figure 3. Considering the clamped zone from Figure 2, when applying the tip loading, the clamped zone has a line of symmetry. Therefore the two symmetric halves act in parallel and only one half needs to be considered (each half accepts half of the tip force). Converse to this, the centre loading does not contain a line of symmetry so the entire clamped zone needs to be evaluated.

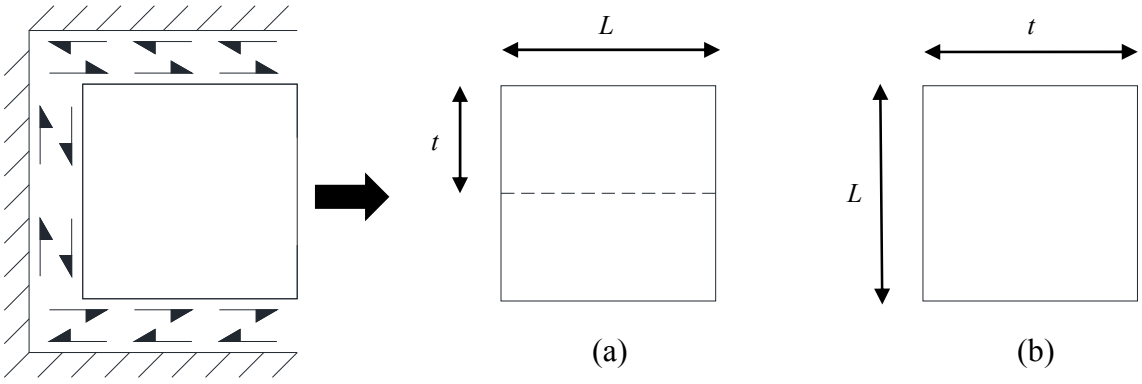

Figure 3: Clamped zone orientation for length, L, and thickness, t, for (a) tip loading and (b) centre loading

Since a symmetric loading is being used, both models will only include the first loading cycle and the completion of the force-displacement hysteresis loop will be achieved using Masing's Rule [8] in this paper.

2.1 Tip loading

The motion caused from the tip loading for the mass in the clamped zone is such that the microslip begins at the edge that is closest to the external mass. The tip loaded microslip model is such that a uniformly distributed clamping load, F_N, is placed on the non-stationary part. The microslip model assumes that the interface always being in full contact over the entire surface and that no overlap is permitted. Unlike microslip from bending, under axial tip loading, the microslip begins at the inception of the applied tip force meaning that no fully sticking contact condition exists. For the first phase, the microslip model is initiated by applying the load from the external mass, F_T, incrementally. The chosen increment size of F_T is important for defining the shape of the hysteresis loop as it relies on a back-looking approach of the displacement of the previous increment of F_T. A graphical representation of the model is shown in Figure 4.

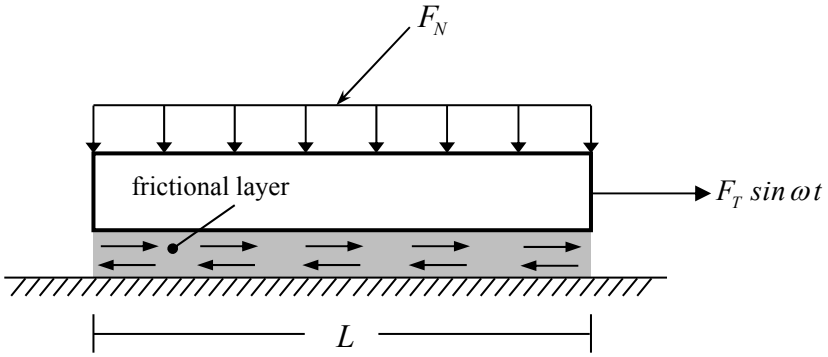

Figure 4: One-dimensional tip loaded axial microslip model

Since F_T is applied perpendicular to F_N, and F_N is distributed over the length of the layer, F_N can then be expressed as a distributed loading along the length such that,

$$q = \frac{F_N \mu}{L}, \tag{2}$$

where L is the length of the clamp zone in Figure 3 and μ is the friction coefficient. Equation 1 implies that for any increment of F_T applied, some amount of slip will immediately be returned. The slip zone for the first iteration is then described by

$$u_{i=1} = \frac{F_{T(i=1)}}{q}. \tag{3}$$

When applying F_N, slipping begins at the edges of the contact area and progresses toward the centre as F_N increases. This slipping is however ignored and is considered to be negligible. Substituting Equation 2 into Equation 3, the slip zone length for the subsequent iterations is expressed as

$$u_i = \frac{F_{T(i)}\left(L + \delta_{x(i-1)}\right)}{F_N \mu}, \tag{4}$$

where δ_x is the axial displacement that is used to update L and the subscript i denotes the increment of F_T. It becomes apparent that macroslipping is initiated once

$$F_T = F_N \mu . \tag{5}$$

Poisson's ratio effects have been included for both the tip and centre microslip models since a no sticking condition is achieved and that the compressive loads could be rather high resulting in high F_T under displacement controlled excitation. Although the volumetric change from Poisson's ratio occurs evenly for each direction, one key assumption that is made is that in the thickness direction, the thickness changes are accumulated only in a single direction. Meaning that any increase and/or decrease in thickness occurs at the top surface of the sample only so that contact is maintained at all times. The depth and thickness are respectively expressed as

$$w_i = w_{i-1} - \left(\frac{\nu w_{i-1} F_{T(i)}}{E w_{i-1} t_{i-1}}\right), \tag{6}$$

and

$$t_i = t_{i-1} - \left(\frac{\nu t_{i-1} F_{T(i)}}{E w_{i-1} t_{i-1}}\right), \tag{7}$$

where v is Poisson's ratio and E is the modulus of elasticity. Once slipping occurs, the friction is fully overcome and the interface behaves as though it is frictionless where slipping is present for the amplitude of force that is being applied that exceeds the friction force. Knowing that the axial stiffness of a uniform cross-section is defined as

$$k = \frac{AE}{L}, \tag{8}$$

where A is the cross-sectional area, substituting Equations 4, 6 and 7 into Equation 8, the axial stiffness of the portion of the bar that is slipping becomes

$$k_i = \frac{w_i t_i 2E}{u_i}. \tag{9}$$

The stiffness in this case is doubled as not only does the slipping have to be overcome but also a load that is necessary to allow for displacement of the slipped zone. Although the microslip resembles a nonlinearity, each displacement is linear. Therefore, the displacement is expressed by

$$\delta_{x(i)} = \frac{F_{T(i)}}{k_i}. \tag{10}$$

2.2 Centre loading

Converse to that from the tip loading, the motion created by the centre loading, for the mass located within the clamped zone, is such that the microslip originates at the centre. The non-stationary sample of the centre loaded microslip model contains a uniformly distributed clamping load, F_N, resembling a

preload. The microslip model is predicated on the interface always being in full contact over the entire surface and that no overlap exists between the sample and the constrained support. Unlike microslip from bending, and similar to axial tip loading, the microslip begins at the inception of the applied centre force resulting in a non-fully sticking contact condition. For the first phase, the microslip model is initiated by applying the load from the external mass, F_T, incrementally. The resolution and accuracy for the shape of the hysteresis loop is defined by the chosen increment size of F_T as it relies on a back-looking approach of the displacement of the previous increment of F_T. A graphical representation of the model is shown in Figure 5.

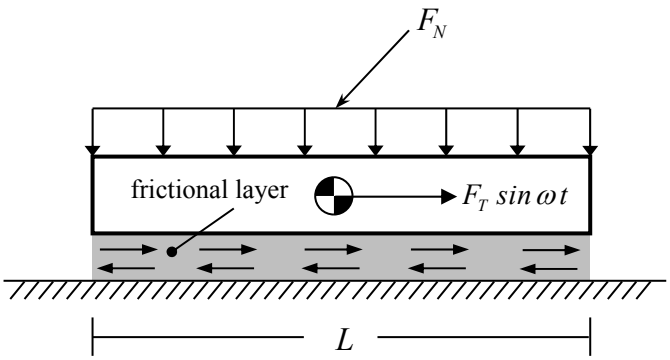

Figure 5: One-dimensional centre loaded axial microslip model

Like the tip loaded microslip model, the same assumptions apply and too when F_N is placed on the non-stationary sample, the microslip caused from it is considered to be negligible and is therefore omitted. Microslip begins when $F_T > 0$, however this now originates at the centre of the sample. Unlike that of the tip loaded microslip model, where the tension and compression occur separately, the compression and tension for the centre loaded microslip model occurs simultaneously for each phase. Consequently, to determine the hysteresis loop, the sample is split at the centre of mass along the length separating the tension and compression domains. Knowing that the slip zone develops from Equation 3 and that F_T is

equally shared between the tension and compression domains, the slip zone of interest for each domain for the first phase is defined as

$$u_{ic,it} = \frac{F_{T(i)}\left(L + \delta_{x(ic-1,it-1)}\right)}{4F_N\mu}, \tag{11}$$

where the subscripts *ic* and *it* define the increment for the compression and tension domains, respectively. For the first increment, $\delta_{x(ic-1,it-1)} = 0$ and the slip zones are equal to one another. Since both tension and compression occur simultaneously, a reduction and an increase in cross-sectional areas occur at once but at different rates. Hence, the Poisson's ratio effects need to be computed for each domain separately. The depth and thickness changes for the compression domain are increasing in cross-sectional area and are expressed as

$$w_{ic} = w + \frac{\delta_{x(ic-1)}wv}{u_{ic-1}}, \tag{12}$$

and

$$t_{ic} = t + \frac{\delta_{x(ic-1)}tv}{u_{ic-1}}. \tag{13}$$

On the other hand, the tension domain is reducing in cross-sectional area so the depth and thickness changes are defined as

$$w_{it} = w - \frac{\delta_{x(it-1)} wv}{u_{it-1}}, \tag{14}$$

and

$$t_{it} = t + \frac{\delta_{x(it-1)} tv}{u_{it-1}}. \tag{15}$$

Now that the Poisson's ratio effects have been included, the stiffness shift for each domain is expressed as

$$k_{ic,it} = \frac{w_{ic,it} t_{ic,it} 2E}{u_{ic,it}}. \tag{16}$$

Following the same format as Equation 10, the displacement for the compression and tension domains are expressed as

$$\delta_{x(ic,it)} = \frac{F_{T(ic,it)}}{k_{ic,it}}. \tag{17}$$

Up to now, the peak displacements that have been computed are related to the restriction of no participation from the other domain. The total peak centre displacement of the system is now expressed as a combination of the peak displacements for each of the domains and is given as

$$\delta_{x(i)} = \frac{\left(k_{ic}\delta_{x(ic)}\right) + \left(k_{it}\delta_{x(it)}\right)}{k_{ic} + k_{it}}. \tag{18}$$

3 Model coupling

To find the overall damping from the two models, for the planar motion in the clamping zone, a coupling between the models is required. In the approach that is listed in this paper, the hysteresis loops for each of the different loadings (tip and centre) are required which are defined from above in the previous sections. The coupling is achieved by vectorially combining the two independent motions to create a resultant hysteresis loop as shown in Figure 6. For clarity, the solid lines indicate the data located in the positive-positive-positive quadrant while the dashed lines are for data in all other quadrants.

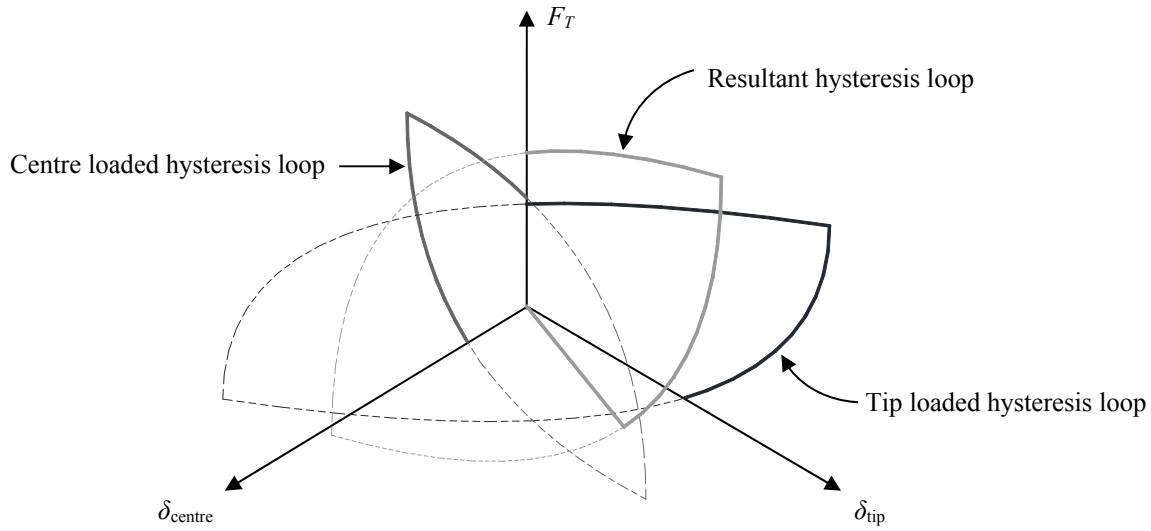

Figure 6: Euclidean space representation for resultant hysteresis loop. For clarity, solid lines indicate the positive-positive-positive octant data and dashed lines represent the remaining octants data.

Once the hysteresis loop for each model is established, the resultant hysteresis displacement can be defined by

$$\delta_{x(ir)} = \sqrt{\delta_{x(it)}{}^2 + \delta_{x(ic)}{}^2} \left(\frac{\delta_{x(it)}}{\left| \delta_{x(it)} \right|} \right), \tag{19}$$

where the subscript *ir* denotes the resultant iteration. In a similar approach, the resultant hysteresis force can also be described by

$$F_{T(ir)} = \sqrt{F_{T(it)}{}^2 + F_{T(ic)}{}^2} \left(\frac{F_{T(it)}}{\left| F_{T(it)} \right|} \right). \tag{20}$$

Once the resultant displacement and force are both found, the resultant hysteresis can then be formed. Using the resultant hysteresis loop, the total absorbed energy, W_d, and peak strain energy, U, can be estimated and is accomplished by

$$W_d = \oint F_{T(ir)} \delta_{x(ir)}, \tag{21}$$

and

$$U = \int_{\delta_{x(ir)}, F_{T(ir)}=0}^{\delta_{x(ir)}, F_{T(ir)}=\sigma} F_{T(ir)} \delta_{x(ir)}, \tag{22}$$

where σ is the peak amplitude. By knowing Eqs. 20 and 21, the damping loss factor is then conventionally described as

$$\eta = \frac{W_d}{2\pi U} . \tag{23}$$

4 Finite element model

ANSYS commercial finite element (FE) code is used as the FE solver. The FE model employs 3-D solid higher-order hexahedron (SOLID186) and 2-D contact elements with approximately 10500 degrees of freedom. Only two different parts are needed for the FE model: a base and a sample. The sample represents the mass that is inside the clamping zone while the base represents the rigid clamp. Contact pairs consisting of contact (CONTA174) and target (TARGE170) elements are used to provide interaction between the mass and clamped zone through the implementation of Coulomb friction. The interpretation of Coulomb friction for ANSYS is that the product of the force normal to the sliding direction and the friction coefficient is a limiting force. If the tangential force is less than the limiting force the state of the contact is sticking. However, if the tangential force is equal or greater than the limiting force then the contact is sliding producing relative motion. An augmented Lagrange contact formulation is used to help with convergence. This method is an iterative series whereby the pressure and frictional stresses are augmented during the equilibrium iterations resulting in the final contact penetration being decreased and lower than the user-defined allowable penetration. This generally leads to better conditioning of the stiffness matrix as compared to other penalty methods. A contact stiffness factor of 1, which is updated for each equilibrium iteration, is used to minimise the amount of penetration between the sample and base. Although the sample is not subjected to large deflections, nonlinear geometry is accounted for to accommodate the sliding of the contact elements. The FE model configuration is shown in Figure 7.

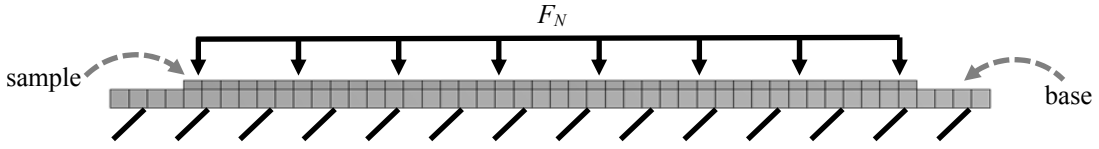

Figure 7: Example FE model for the mass and clamp zone

A single loadstep was used for each simulation comprised of a sinusoidal load applied over a duration equal to 125% of the frequency period (1Hz was used in this paper). The first 25% of the period moves the sample from rest into the hysteresis loop path while the remaining 100% of the period completes a loop. To help with convergence further, and to gain meaningful and comparable results with the tip and centre loaded models, the tip and centre loads were discretised into 50 linearly-spaced substeps. The size of the substeps is dependent on several factors (e.g. mesh, deformation). However, possibly the most important of them being the contact element mesh density. The mesh density needs to be sufficient to capture the stick-slip of the contact region. Each substep was then split into a maximum of 26 equilibrium iterations while outputting the Newton-Raphson residuals for convergence checking.

As also noted in the tip model, when the tip force is initiated, the contact zone of the tip breaks free firstly while propagating to the root end of the sample. In a similar way, when the centre load is firstly applied to the centre model, the centre contact zone of the sample commences slipping and extends toward the edges as the load increases. The slip growth for the various loading and unloading phases is illustrated in Figure 8.

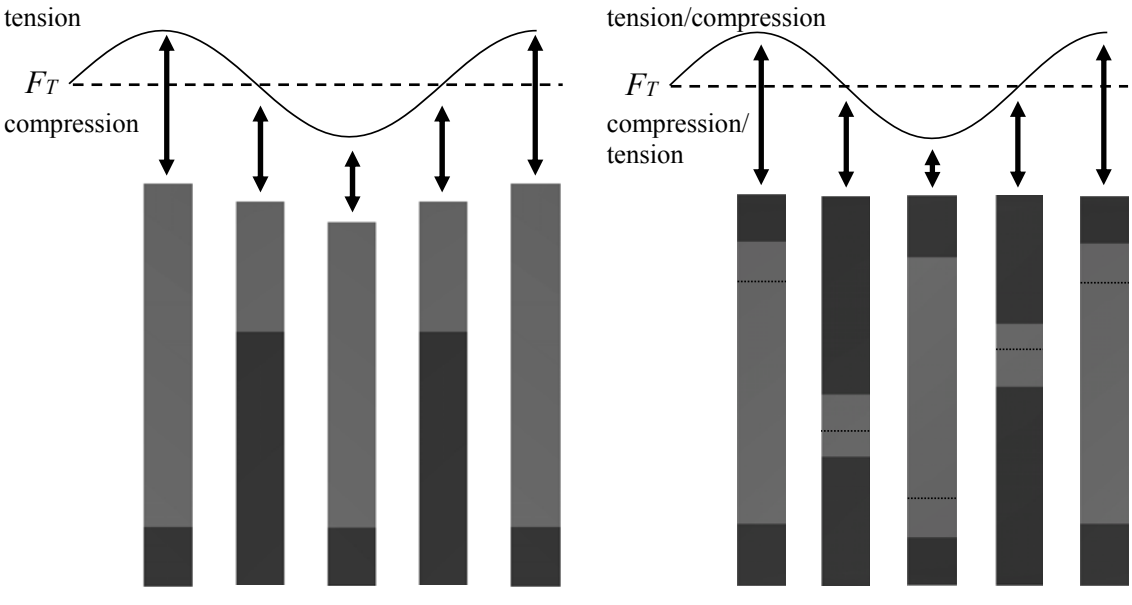

(a) (b)

Figure 8: Typical contact status and exaggerated deformations from FE simulation for various loading and unloading phases for (a) tip loading and (b) centre loading

Figure 8 shows the sticking (dark grey) and slipping (light grey) regions at the end of each 90° for the sequential tip and centre harmonic loading. For the tip loading, the bottom-most portion is constrained while the top-most portion is where F_T is applied. It is clear that when tension loading the portion of the layer that is slipping is elongated and that as the slip zone decreases, the stiffness is increased and that the elongation is reduced. For the centre loading, the black lines indicate the displaced position of $L/2$. It is clear that unlike the tip loading, the overall length of the layer remains constant since the loading is confined to the microslip region and is in the centre.

5 Results and discussion

A total of seven unique loading eccentricities were used as depicted in Figure 1. To validate the accuracy and propriety of the mathematical models, numerical models using FEs are used as a comparison. For the ease and interest of reducing computational time, for the nonlinear simulations, the comparisons are made using a simplified geometry. The geometry, material properties and parameters used for the simulations are given in Table 1 where ν is Poisson's ratio and μ is the friction coefficient.

L (mm)	w (mm)	t (mm)	E (MPa)	ν	μ	F_N (N)	F_T (N)
254	25.4	3.18	68947	0.3	0.8	445	267

Table 1: Simplified geometry, properties and parameters

Although this geometry has been simplified, it still contains all of the important aspects of the actual clamped joint. The comparison between the mathematical model and numerical model, for the tip loading and centre loading, are given in Figure 9a-b, respectively. To balance the accuracy of the FE model and the computational time, the contact mesh adequacy was defined in these simulations as a difference in contact sliding distance as less than 0.5%.

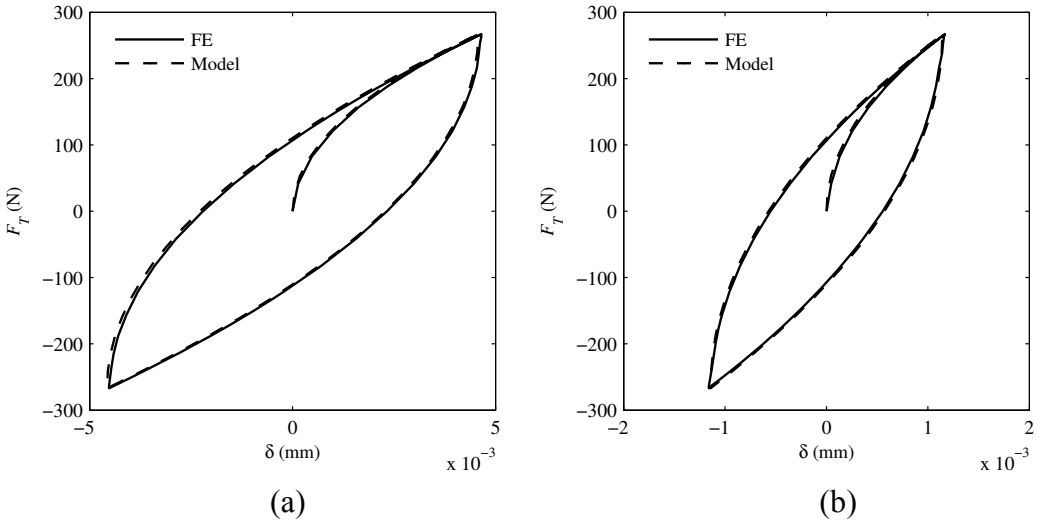

Figure 9: FE and mathematical model comparison for (a) tip loading and (b) centre loading

For the example joint that is used in this paper, for the comparison of various eccentricities for the mathematical models, the joint geometry along with the properties and parameters are identified in Table 2. The amplitude of F_T that is applied to the tip model is 2000N, 4000N, 6000N and 8000N and for the

centre model 4000N, 8000N, 12000N and 16000N. The F_T for the tip model is half that of the centre model since symmetry is being used.

model	L (mm)	w (mm)	t (mm)	E (MPa)	v	μ	F_N (N)
tip	50	10	25	10000	0.3	0.8	20000
centre	50	10	50	10000	0.3	0.8	20000

Table 2: Respective joint geometries, properties and parameters

The results for each of the circular and elliptical force ratios and eccentricities, defined from Figure 1, are shown in Figures 10 (R=1, 2, 3 and 4) and 11 (R=1, 0.50, 0.33, 0.25). It is noticed that as F_T is increased for each of the models, the stiffness decreases having a softening effect. It is also obvious from Figure 8a that the stiffness of the centre model is greater than that of the tip model.

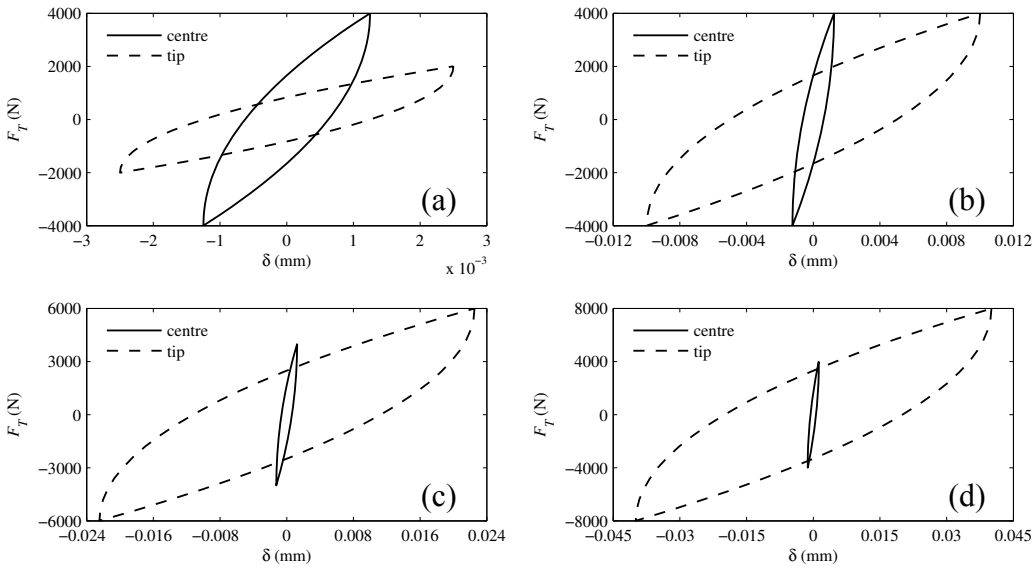

Figure 10: Tip and centre loading force-displacement hysteresis loops for (a) R=1, ε=0, (b) R=2, ε=0.86, (c) R=3, ε=0.94 and (d) R=4, ε=0.97

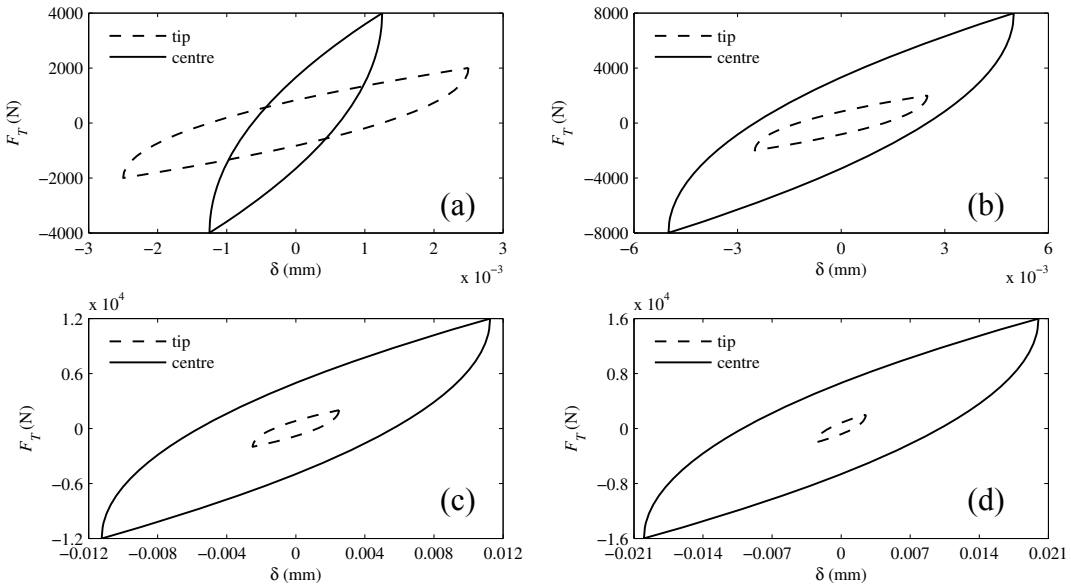

Figure 11: Tip and centre loading force-displacement hysteresis loops for (a) R=1, ε=0, (b) R=0.5, ε=0.86, (c) R=0.33, ε=0.94 and (d) R=0.25, ε=0.97

The normalised vibration damping loss factor for the different forcing ratios (eccentricities) is shown in Figure 12. Interestingly the highest damping loss factors are at the extreme elliptical motion. This is directly associated with the combination of the ellipticity and the increase in F_T. This information follows the findings by Hartwigsen et al [1].

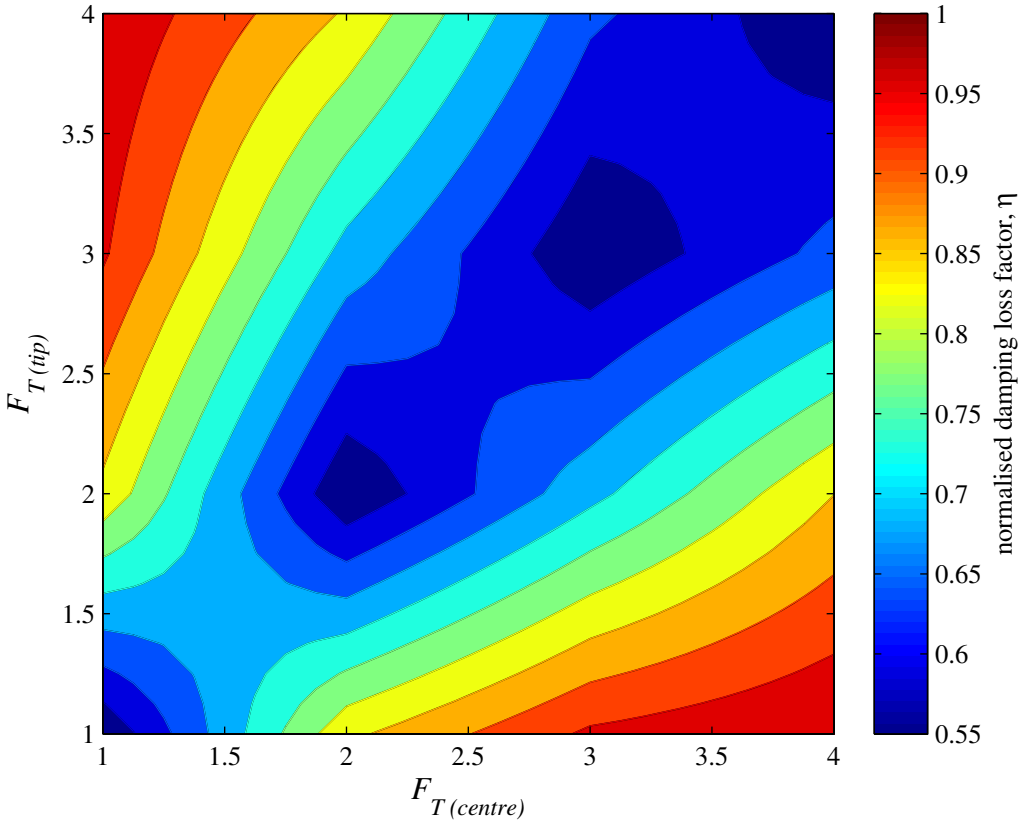

Figure 12: Normalised damping loss factor for various R

It is noticed from Figure 12 that when R=1, the loss factor is the lowest. Conversely, when R is minimum and maximum (R=0.25 and R=4), the loss factor is the largest. Additionally, the gradient of the slope between for the damping loss factor changes as R increases and decreases pivoting around R=1.

6 Conclusions

Two different tangential microslip models (tip and centre loaded) have been presented. Each model is capable of producing force-displacement responses. Both models are compared to FE models and have shown good agreement between the mathematical and numerical results. Using a coupling approach, the

two microslip models are combined to demonstrate the overall response for the normalised damping loss factor for various two-dimensional trajectories

Acknowledgements

This research received no specific grant from any funding agency in the public, commercial, or not-for-profit sectors.

References

[1] Hartwigsen, C.J.; Song, Y.; McFarland, D.M.; Bergman, L.A.; Vakakis, A.F.. Experimental study of non-linear effects in a typical shear lap joint configuration, *Journal of Sound and Vibration*, 2004, 277, 327-351.

[2] Menq, C.H.; Bielak, J.; Griffin, J.H. The influence of microslip on vibratory response, part I: A new microslip model, *Journal of Sound and Vibration*, 1986, 107(2), 279-293.

[3] Menq, C.H.; Griffin, J.H.; Bielak, J. The influence of microslip on vibratory response, part II: A comparison with experimental results, *Journal of Sound and Vibration*, 1986, 107(2), 295-307.

[4] Cigeroglu, E.; Lu, W.; Menq, C.H. One-dimensional dynamic microslip friction model, *Journal of Sound and Vibration*, 2006, 292, 881-898.

[5] Xiao, H.; Shao, Y.; Xu, J. Investigation into the energy dissipation of a lap joint using the one-dimensional microslip friction model, *European Journal of Mechanics A/Solids*, 2014, 43, 1-8.

[6] Sanliturk, K.Y.; Ewins; D.J. Modelling two-dimensional friction contact and its application using harmonic balance method, *Journal of Sound and Vibration*, 1996, 193(2), 511-523.

[7] Menq, C.H.; Chidamparam, P.; Griffin, J.H. Friction damping of two-dimensional motion and its application in vibration control, *Journal of Sound and Vibration*, 2004, 144(3), 427-447.

[8] G. Masing. Eigenspannungen un verfestigung beim messing. *Second International Congress for Applied Mechanics*, 332-335, 1926.